



Improving heterogeneous photo-Fenton catalytic degradation of toluene under visible light irradiation through Ba-doping in BiFeO₃ nanoparticles



Tayyebeh Soltani, Byeong-Kyu Lee*

Department of Civil and Environmental Engineering, University of Ulsan, Nam-gu, Daehak-ro 93, Ulsan 680-749, Republic of Korea

ARTICLE INFO

Article history:

Received 15 August 2016

Received in revised form

23 September 2016

Accepted 5 October 2016

Available online 15 October 2016

Keywords:

Toluene

Ba doped BFO

Heterogeneous photo-Fenton catalysis

mechanism

XPS spectroscopy

ABSTRACT

In this study, we prepared Bi_{1-x}Ba_xFeO₃ MNPs ($x = 0.03, 0.08, 0.12$) via a rapid sol gel procedure to improve heterogeneous photo-Fenton catalytic degradation of toluene under visible light irradiation. We found that Ba-substitution in BiFeO₃ magnetic nanoparticles (BFO MNPs) can play an important role in improving the photo-Fenton catalytic degradation of toluene from aqueous solution. Increasing the Ba doping level up to 12%, greatly affect in iron redox cycling and oxygens vacancies as compared to pure BFO MNPs. The iron redox cycling and existence of oxygen on the surface of Ba doped BFO had been affected by the photo-Fenton process. The scavenger effect evident from the study results confirmed that the photo-Fenton catalytic degradation of toluene from aqueous solution was mainly controlled by the formation characteristics of hydroxyl radical ($\cdot\text{OH}$) and also partially by the formation of other active species such singlet oxygen (${}^1\text{O}_2$). The proposed radical reaction mechanism was also discussed. The degradation of toluene was partial in the dark but almost complete under visible light irradiation by the photo-Fenton catalytic degradation reaction. Bi_{1-x}Ba_xFeO₃ ($x = 0.12$) showed the highest photo-Fenton catalytic degradation efficiency with a toluene removal of 98%, total organic carbon (TOC) and chemical oxygen demand (COD) reduction of 85% and 94%, respectively, after 40 min of visible light irradiation.

© 2016 Elsevier B.V. All rights reserved.

1. Introduction

Volatile and flammable aromatic hydrocarbons such as benzene, toluene, ethylbenzene and xylene have commonly been used in solvents and exist in fossil fuels such as gasoline and petroleum [1,2]. Long-term exposure to volatile organic compound (VOCs) may cause serious problems such as a wide range of sensory irritation and acute or chronic diseases.

Various methods have been developed for eliminating VOCs [3–5]. Among advanced oxidation processes, Fenton (Fe(II)/H₂O₂) and photo-Fenton (Fe(II)/H₂O₂/UV) reagents have been used in a lot of wastewater purification processes due to their favorable organic treatment efficiency [6]. However, homogeneously catalyzed Fenton reactions require higher concentrations of aqueous iron ions than the 2 ppm permitted by the European Community Directives [7]. Thus, it has essential requirements for precipitation, re-dissolution, separation and recovery of the iron species especially in industrial wastewater treatment due to a large amount

of iron salts that are presented in the effluents. In heterogeneous catalysis, iron is perched within the interlayer space of the catalyst's structure and can effectively generate hydroxyl radicals ($\cdot\text{OH}$) from the oxidation of hydrogen peroxide (H₂O₂), without iron hydroxide precipitation under non-controlled pH conditions [8,9].

BiFeO₃ magnetic nanoparticles (BFO MNPs) belong to the ABO₃ type of compounds with a rhombohedral distorted perovskite structure, which is a new visible-light photocatalyst for the photo degradation of organic pollutants because of its narrowing band gap energy (2.2 eV), magnetic property and excellent chemical stability [10–12]. Multi-ferroic BFO MNPs were used as a catalyst for ultrasensitive fluorometric determination of hydrogen peroxide and glucose [13]. BFO MNPs are able to catalytically activate H₂O₂ for the decomposition of organic pollutants in the dark, but their catalytic ability for more resistant organic pollutants is rather weak [14]. Thus, visible light irradiation can be utilized to improve the catalytic ability of BFO MNPs [9,15]. However, the catalytic ability of BFO MNPs was not enough to degrade more stable organic pollutants, such as bisphenol A and methyl violet, from aqueous solution. Therefore, it was necessary to improve the catalytic ability of BFO MNPs by an in-situ surface modification using chelating agents such as ethylenediaminetetraacetic acid (EDTA) [16,17]. Recently, it was

* Corresponding author.

E-mail address: bklee@ulsan.ac.kr (B.-K. Lee).

reported that the BFO lattice undergoes a large structural distortion even at a low concentration of Li doping [18]. It has been reported that the substitution of Ca and Sr for Bi induced oxygen vacancies and mixed Fe valences, which can play an important role in the photocatalytic property of BFO MNPs [19,20].

In this study, we prepared $\text{Bi}_{1-x}\text{Ba}_x\text{FeO}_3$ MNPs with different Ba^{2+} ion-dopant levels ($x=0.03, 0.08, 0.12$) via a rapid sol gel procedure to improve heterogeneous photo-Fenton catalytic degradation of toluene under visible light irradiation. For the first time, we found that Ba substitution in BFO MNPs greatly improved the photo-Fenton catalytic degradation of toluene at a very weak acidic medium, $\text{pH}=5.5$, due to greatly affect in iron redox cycling and oxygens vacancies as compared to pure BFO MNPs. The iron redox cycling and existence of oxygen on the surface of Ba doped BFO had been affected after photo Fenton process. Finally, we found that, singlet oxygen was partly exhibited roles in the photo-Fenton catalysis process of toluene in addition to $\cdot\text{OH}$, and relevant radical reaction mechanism was also proposed.

2. Materials and methods

2.1. Chemicals

Bismuth nitrate ($\text{Bi}(\text{NO}_3)_3 \cdot 5\text{H}_2\text{O}$), iron nitrate ($\text{Fe}(\text{NO}_3)_3 \cdot 9\text{H}_2\text{O}$), barium nitrate ($\text{Ba}(\text{NO}_3)_2$), and H_2O_2 from Fluka, ethylene glycol (EG), isopropanol (IP), sodium azide (NaN_3) and 1–4 benzoquinone (BQ) from Merck, and toluene and ethanol from Aldrich were used as received.

2.2. Catalyst preparation

To synthesize pure BFO MNPs, 25 mmol of $\text{Bi}(\text{NO}_3)_3 \cdot 5\text{H}_2\text{O}$ and $\text{Fe}(\text{NO}_3)_3 \cdot 9\text{H}_2\text{O}$ were dissolved in 65 mL EG. The mixture was stirred for 40 min at 30°C to obtain a dark red sol. For the preparation of $\text{Bi}_{1-x}\text{Ba}_x\text{FeO}_3$ ($x=0.03, 0.08, 0.12$), $\text{Bi}(\text{NO}_3)_3 \cdot 5\text{H}_2\text{O}$, $\text{Fe}(\text{NO}_3)_3 \cdot 9\text{H}_2\text{O}$ and $\text{Ba}(\text{NO}_3)_2$ were added to the EG at a molar ratio of $1-x: 1: x$; where $x=0.03, 0.08$ and 0.12 for 3%, 8%, and 12% Ba doped samples, respectively. Then, samples irradiated for 40 min at 30°C to obtain other brownish red sols. Then, all samples were incubated at 80°C to 20 h to remove the organic pollutants and to form xerogels. Finally, the powders were calcined at 500°C for 1 h at a heating rate of $6^\circ\text{C}/\text{min}$ to afford pure BFO and Ba doped BFO MNPs, respectively.

2.3. Degradation experiments

This study focuses on the application of the photo-Fenton catalytic degradation of toluene from aqueous solutions using undoped and Ba doped BFO MNPs. Before irradiation, the suspension was magnetically stirred for 45 min in a dark place and then irradiated for different time intervals at a fixed temperature of 25°C by using a water bath. The photo-Fenton catalytic degradation of toluene was carried out under the irradiation of a 55 W fluorescent lamp at a distance of 15 cm with an emission peak at 550 nm under continuous magnetic stirring. For photo-Fenton catalytic degradation of toluene under visible light irradiation, photocatalyst powder (40–mg) and 0.6–65 mM H_2O_2 were added into 100 mL of toluene solution (100 mg L^{-1}) in a 250 mL Erlenmeyer flask with an appropriate cap to stop evaporation of toluene solution during photodegradation process. After reaction completion, the photocatalyst was easily separated from the solution by using an external magnetic field. The concentration of the toluene solution was evaluated by measuring the intensity of the absorption

peak at 205 nm using a UV-vis spectrophotometer. The conversion of toluene was defined as the following Eq. (1):

$$\text{Conversion} = \left[\frac{\text{C}_0 - \text{C}}{\text{C}_0} \right] \times 100 \quad (1)$$

Where C_0 is the initial concentration of the toluene solution and C is the concentration of toluene remaining in the solution after the photocatalytic reaction.

Furthermore, a blank solution (without the photocatalyst) was used in all experiments to evaluate the amount of toluene evaporation. Toluene evaporation during the photo degradation process was negligible when a cap was used

2.4. Characterization equipment

The crystalline structure was identified by using X-ray diffraction (XRD) (BrukerD8Advance) with monochromatic $\text{Cu K}\alpha$ radiation ($\lambda=1.5406\text{ \AA}$). The samples' morphology and size were examined by transmission electron microscopy [(TEM, JEOL TEM Model 2100)]. To analyze the chemical states of the constituents, X-ray photoelectron spectroscopy (XPS) was conducted with a Thermo Scientific Sigma Probe spectrometer with a monochromatic $\text{Al K}\alpha$ source (photon energy 1486.6 eV), spot size 400 μm , pass energy 200 eV and energy step size 1.0 eV. A Genesis 10S UV-vis spectrophotometer was used to obtain the absorbance of toluene at λ_{max} of 205 nm. The chemical oxygen demand (COD) test was used to express the COD of toluene solution. The total organic carbon (TOC) of the toluene solution was determined by TOC 500 A (Shimazu, Japan).

3. Results and discussion

3.1. Characterization of the catalyst

3.1.1. XRD results

XRD patterns of as-prepared pure BFO and Ba doped BFO samples with varying content of Ba are shown in Fig. 1. All XRD peaks corresponding to BFO perovskite structure with R3c space group (JCPDS No. 86-1518), demonstrating that single crystalline BFO MNPs phase. The rhombohedral structure of BFO MNPs does not change appreciably with Ba doping, except increase in $\text{Bi}_{25}\text{FeO}_{39}$ impurity phases. From a small magnified section of XRD patterns in the 2θ range of 31–33, it is clear that the (104) and (110) peaks split for pure BFO MNPs and it was merged into a single (110) peak, arising from the substitution of larger ionic radius of $\text{Ba}^{2+}(1.36\text{ \AA})$ than that of $\text{Bi}^{3+}(1.17\text{ \AA})$. The calculated crystalline sizes using Scherer's formula were found to be 33, 23 nm, 31.7 nm and 30.1 nm for pure BFO, Ba 8%–BFO and Ba 12%–BFO, respectively. Compared with the pure BFO MNPs, with increasing the Ba doping content, the crystalline size of Ba doped BFO slightly decreased, revealing the structural distortion of BFO induced by the Ba doping.

3.1.2. XPS results

Further evidence for the quality and composition of the BFO and Ba doped BFO MNPs was obtained from XPS studies. The survey spectra from 0 to 1000 eV for pure and Ba doped BFO MNPs as shown in Fig. 2 confirm the presence of Bi, Fe, O and minor quantities of Ba for $\text{Bi}_{1-x}\text{Ba}_x\text{FeO}_3$ ($x=0.03, 0.08$ and 0.12), without traces of any other impurities and with the exception of a small amount of adsorbed carbon peak C 1s at 285 eV to calibrate the system. Furthermore, in the pure BFO MNPs, the molar ratio of bismuth, iron and oxygen is almost 1:1:3. However, in the Ba doped BFO MNPs samples, the amounts of Ba identified by the XPS analysis were a little less than those actually added in the synthesis. The detected atomic fractions of Ba in Ba doped BFO MNPs were 2.8, 7.5 and 11.6

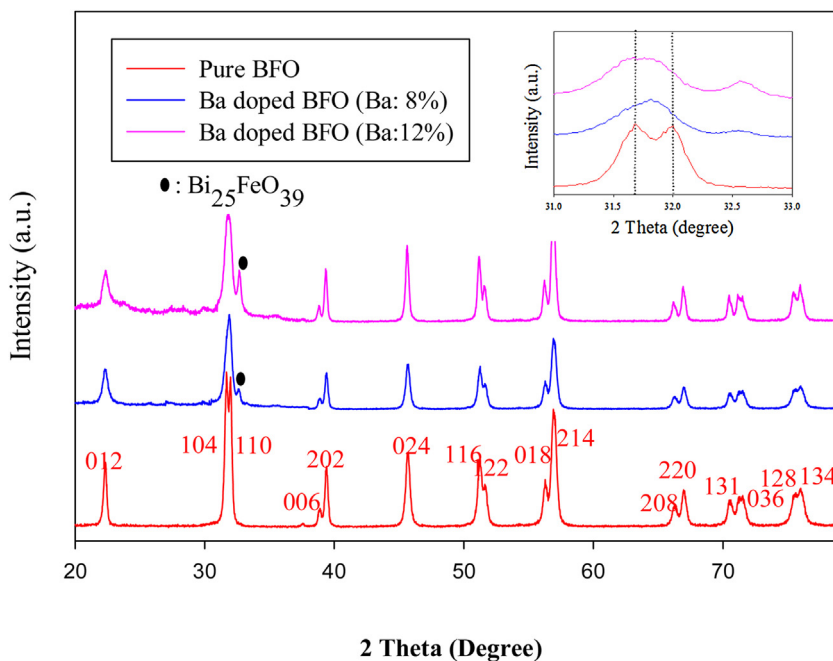


Fig. 1. XRD patterns for Bi_{1-x}FeO₃ MNPs ($x = 0, 0.08, 0.12$); insets show the patterns of the main peak near 32° in BFO and Ba doped BFO MPNs samples.

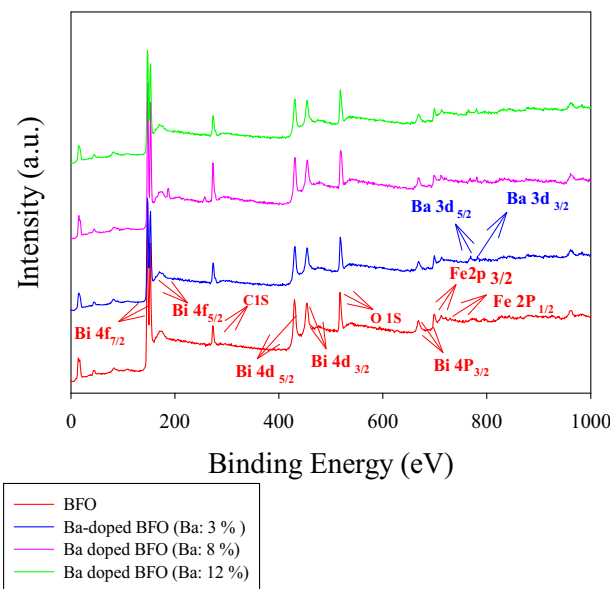


Fig. 2. XPS survey spectra of Bi_{1-x}FeO₃ MNPs ($x = 0, 0.03, 0.08, 0.12$).

in at.%, which are slightly lower than those (3, 8 and 12%) actually added in the synthesis, respectively.

To further measure the oxidation states of Fe and oxygen with Ba doping, high resolution XPS spectral analyses of Fe 2P_{3/2} were performed for pure BFO and Ba doped BFO as shown in Figs. 3 and 4, respectively. In the high resolution XPS of Fe 2P_{3/2} (Fig. 3), the binding energies of Fe 2P_{3/2} at 709.2 eV and 711.1 eV correspond to Fe²⁺ and Fe³⁺, respectively. The fitting results of the peaks for the valence states of Fe ions revealed that the almost Fe³⁺ exists in the structure of pure BFO MNPs. As shown in Fig. 3b and c, Fe²⁺ and Fe³⁺ simultaneously existed in Bi_{1-x}Ba_xFeO₃ MNPs ($x = 0.03, 0.08$). However, the high proportion of Fe²⁺ to Fe³⁺ species becomes remarkably pronounced for these samples. However, the binding energy for Fe 2P_{3/2} was completely shifted from 711.1 eV for the pure BFO to 709.2 eV for the Ba doped BFO MNPs ($x = 0.12$). The main rea-

son for the binding energy shift with conversion of Fe³⁺ into Fe²⁺ after Ba doping is that the substitution of Ba²⁺ for Bi³⁺ sites in BFO MNPs creates some defects due to their unequal electrical charge, leading to the generation of some oxygen vacancies and Fe²⁺ to keep electrovalent equilibrium [21]. A clear change in the ratio of Fe²⁺ to Fe³⁺ species after Ba substitution claimed that the photo-Fenton catalytic activity of toluene mainly affected from Fe²⁺ and Fe³⁺ species in Ba doped BFO MNPs.

Similar to Fe 2P_{3/2}, the O 1s peak of pure BFO MNPs undergoes clear variations after Ba substitution. As shown in Fig. 4, oxygen O 1s spectra were fitted roughly with two peaks, O (I) and O (II). O (I) with binding energies around 528.6 eV is the characteristic of lattice oxygen, while O (II) with binding energies around 531.9 eV is mainly related to the absorbed oxygen or defect-oxide [22]. At low level of Ba doping (3%), high proportion of lattice oxygen at 528.60 eV, while low proportion of absorbed oxygen or defect-oxide are presented at 531.9 eV can be seen (Fig. 4b). The reduced proportion of oxygen vacancies at the low concentration of Ba-substitution (3%), is due to the filling the plausible vacant by volatilized Bi³⁺ [21]. However, the proportion of oxygen vacancies was increased as the Ba doping level was further increased up to 12%. The main reason for high proportion of oxygen vacancies with increasing of Ba doping is due to the neutralization of the charges produced by substituting Ba²⁺ for Bi³⁺ [21]. An increase in the number of surface vacancies and defects due to Ba substantiation, rolled as active centers to capture photo-induced electrons and accelerates the photo-Fenton catalytic degradation of toluene with generation of further •OH.

XPS spectral analyses of Fe 2P_{3/2} and O1s represented that with the increase in Ba²⁺ content at the Bi site, relative contribution of Fe²⁺ and oxygen vacancies increased. The maximum proportion of Fe^{2+:} Fe³⁺ and oxygen vacancies can be observed in the 12% Ba doped BFO MNPs.

3.1.3. TEM analysis

Fig. 5 shows morphological investigations of undoped and Ba doped BFO MNPs using TEM. Nanoparticles of nearly spherical morphology with high agglomeration has been observed for undoped and Ba doped BFO MNPs, similar to the others reports [23]. High agglomeration in BFO synthesized nanomaterials is related to high

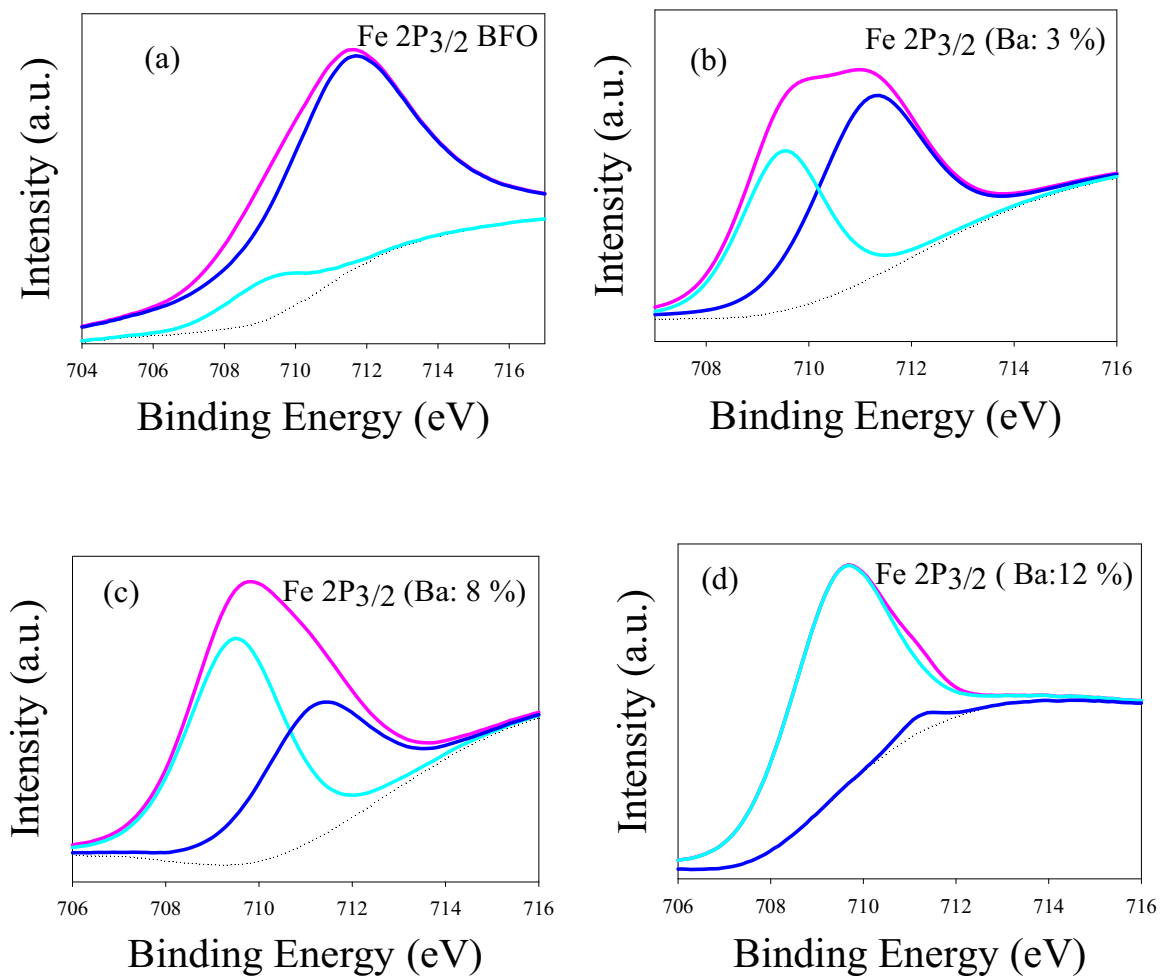


Fig. 3. Fe 2p lines of (a): BFO, (b): 3% Ba doped BFO, (c): 8% Ba doped BFO, and (d): 12% Ba doped BFO MNPs.

surface energy of nanoparticles [23] due to their high surface to volume ratio and magnetic interactions [24]. The average particle size obtained from TEM images for the undoped BFO sample was around 15–20 nm. However, there is no obvious change in particle size of 12% Ba doped BFO compared with the undoped BFO sample.

3.2. Decomposition of toluene

3.2.1. Effect of heterogeneous undoped and Ba doped BFO MNPs

The catalytic performance of undoped and Ba doped BFO MNPs with various Ba doping level, in photo degradation of toluene in the presence of H_2O_2 is shown in Fig. 6. Only 1.5–2% degradation was observed in the absence of the photocatalyst, either under dark or visible light illumination. This indicates that physical adsorption or photolysis were not effective for degradation of toluene, and the presence of BFO MNPs or Ba doped BFO are necessary in the removal process of toluene. After this step, solutions were stirred for 45 min in the dark and then were placed in the presence of visible light irradiation. During dark stirring for 45 min, partial degradation or adsorption took place on the surface of BFO or Ba doped BFO MNPs samples. In the presence of visible light irradiation, however, the catalytic performance for all samples greatly increased in comparison with that in the dark. In the presence of visible light, the amount of radical species generated from the H_2O_2 decomposition was increased [9]. Also, the Ba doped BFO MNPs exhibited higher photo catalytic degradation of toluene than the pure BFO MNPs (59%). By 3% Ba doping, the toluene photo degradation was increased to 70% as compared to pure BFO (59%). When the Ba dop-

ing was increased to 8 and 12%, toluene degradation efficiency was significantly increased to 84 and 98%, respectively. However, there was a slight decline in degradation degree with further increasing the Ba content up to 15%. Thus, Ba loading of 12% showed higher degradation rate than those of 3%, 8% and even 15% Ba loading.

There are some reasons to increase the catalytic degradation of toluene with Ba doping. The perovskite structures are flexible and allow a distortion or induce metastability with the existence of an oxygen vacancy [25]. The presence of oxygen vacancies and defects as active sites on the surface of Ba doped BFO MNPs can accelerate the photo-Fenton catalytic degradation with generation of further $\cdot\text{OH}$ [26]. Furthermore, oxygen vacancies and defects can become active centers to capture photo-induced electrons, which can improve the photo-Fenton efficiency of toluene in the visible region [26]. The substitution of aliovalent elements such as Sr^{2+} , Ni^{2+} , Ca^{2+} , Ba^{2+} , ions [27,28], at the trivalent Fe-site or Bi-site in BFO MNPs, can easily affect the number of holes or electron carriers and oxygen vacancies, which are important intermediates in catalytic degradation of organic pollutants [29,30]. Another reason for the increased degradation with Ba doping is because the recombination of photo-induced electrons and holes can be effectively inhibited during the photocatalytic reaction process. Ba doping brings many new states of energy levels into BFO MNPs as compared with those in BFO MNPs [31]. Thus, the charge separation process can be easily facilitated by minimizing the recombination of electron-hole pairs via transferring of the photo-induced electrons onto the surface of Ba doped BFO MNPs. The slight decrease in toluene removal

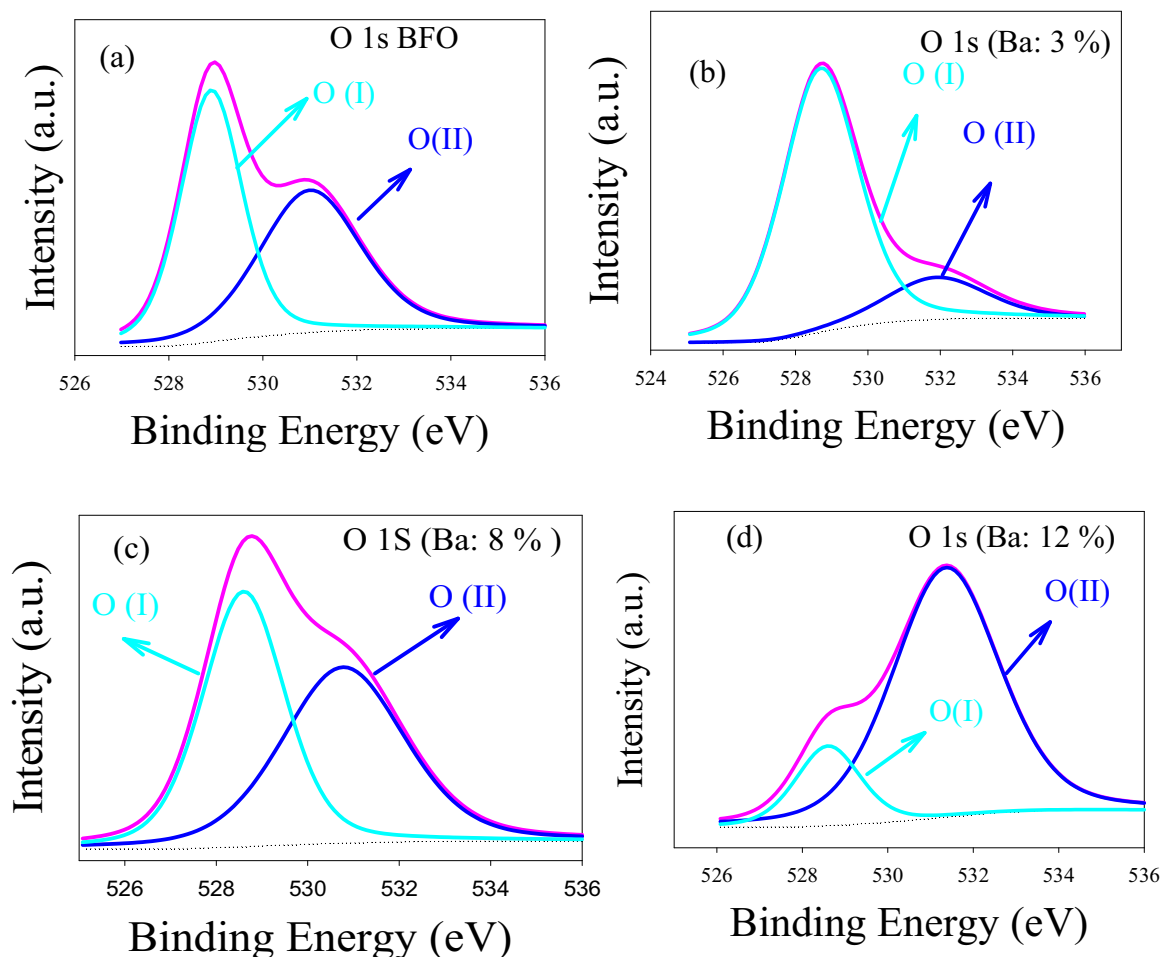


Fig. 4. O 1s lines of (a): BFO, (b): 3% Ba doped BFO, (c): 8% Ba doped BFO, and (d): 12% Ba doped BFO MNPs.

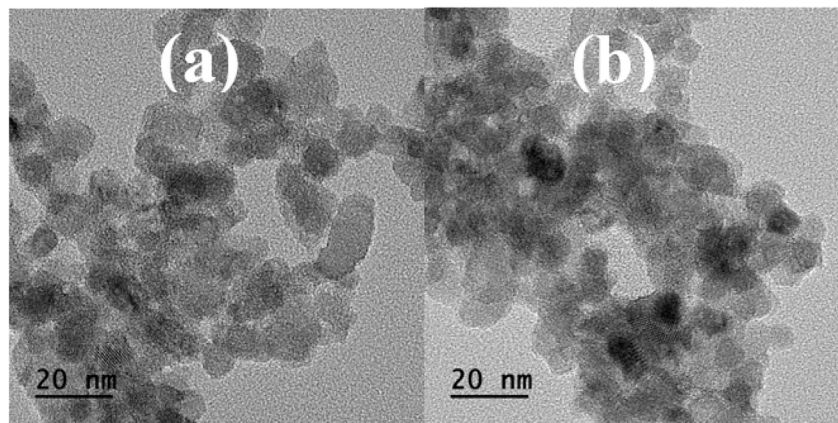


Fig. 5. TEM images of (a) pure BFO MNPs (b) 12% Ba doped BFO MNPs.

at 15% Ba doping may be attributed to suppression of $\cdot\text{OH}$ due to entrapment of conduction band electrons by the adsorbed Ba ions.

3.2.2. Photo-Fenton catalysis processes

The degradation of 100 mg L^{-1} toluene in aqueous solutions under different conditions was performed by using 12% Ba doped BFO as a photo-Fenton catalyst (Fig. 7). When the solution of toluene in the presence of only H_2O_2 (without 12% Ba doped BFO) was irradiated under visible light for 60 min, little degradation was identified. This indicated that toluene can be degraded so slightly,

directly by visible light irradiation in the presence of only H_2O_2 . Hence, subjecting the toluene solution to visible light irradiation cannot induce the photochemical dissociation of H_2O_2 to active species so much. When the toluene solution was stirred in the dark for 45 min, partial degradation with opening or adsorption of the aromatic ring took place on the surface of Ba doped BFO, leading to the disappearance of some of the toluene peak. Partial degradation of toluene in the dark reveals the generation of polycarboxylic acid intermediates with the opening of the aromatic ring in toluene via activation of H_2O_2 by restricting the amount of available $\cdot\text{OH}$

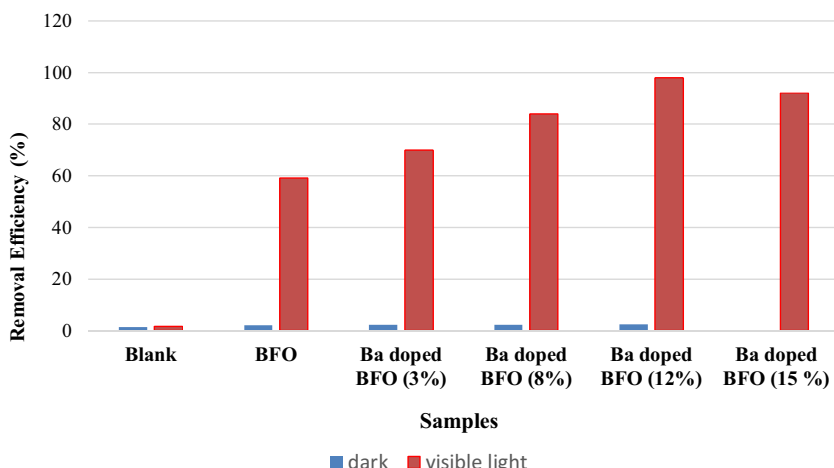


Fig. 6. Effect of the undoped and Ba doped BFO MNPs on the catalytic degradation of toluene. ($t = 25^\circ\text{C}$, time of irradiation: 50 min, $\text{CO}(\text{toluene}) = 100 \text{ mg L}^{-1}$, initial pH = 5.5).

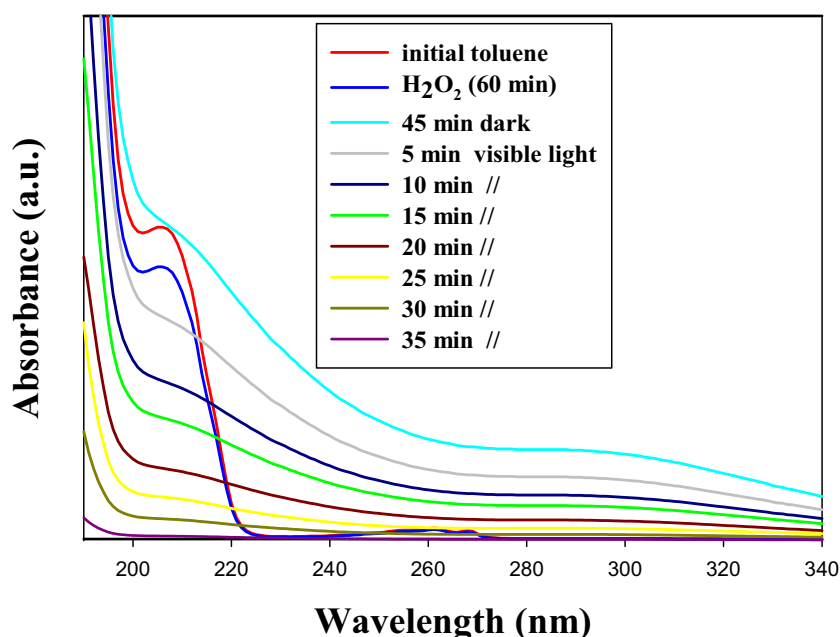
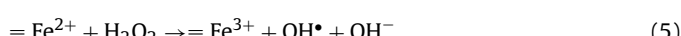
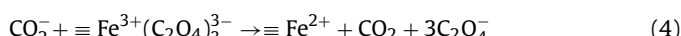
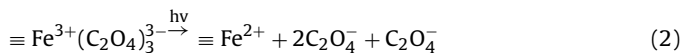


Fig. 7. UV-vis absorption spectra of toluene solution at different contact times with 12% Ba doped BFO MNPs. ($t = 25^\circ\text{C}$, $\text{CO}(\text{toluene}) = 100 \text{ mg L}^{-1}$, $\text{CO}(\text{H}_2\text{O}_2) = 0.6 \text{ mM}$, initial pH = 5.5).

in the dark [32,33]. After 45 min in the dark, the toluene solution was subjected to visible light irradiation for different interval times. In the presence of visible light, the yield of Fe^{2+} greatly increases when Fe^{3+} is complexed with carboxylic anion, such as oxalate ion [44,45], which is formed in dark as an intermediate. The ferrioxalate complex $\equiv \text{Fe}^{3+}(\text{C}_2\text{O}_4)^{3-}$ is highly photosensitive and it is used as the basis of well-known chemical actinometer in photo-Fenton reactions. The reduction of $\equiv \text{Fe}^{3+}$ to $\equiv \text{Fe}^{2+}$ through a photo-induced charge transfer ligand to metal can occur over the ultraviolet-visible region, as shown in Eqs. (2)–(5) [34].



Thus, with increasing irradiation time, the specific absorption peak of toluene during the dark period was gradually reduced and finally disappeared after 35 min as shown in Eq. (6).



3.2.3. Mineralization efficiency

Fig. 8 shows that the variations of toluene degradation efficiency, TOC and COD during the photo-Fenton catalytic degradation after different visible irradiation times. The maximum toluene degradation efficiency, COD and TOC reduction after 40 min of visible light irradiation were about 98%, 94% and 85%, respectively. These results demonstrated the highly efficient mineralization of toluene during the catalysis process.

3.2.4. Radical scavengers

Some radical scavenger experiments were designed to prove the proposed mechanism of toluene degradation with $\cdot\text{OH}$ (Fig. 9). When isopropanol (IP), a popular radical scavenger for $\cdot\text{OH}$ [35,36], was added to the reaction solutions, the toluene photodegradation

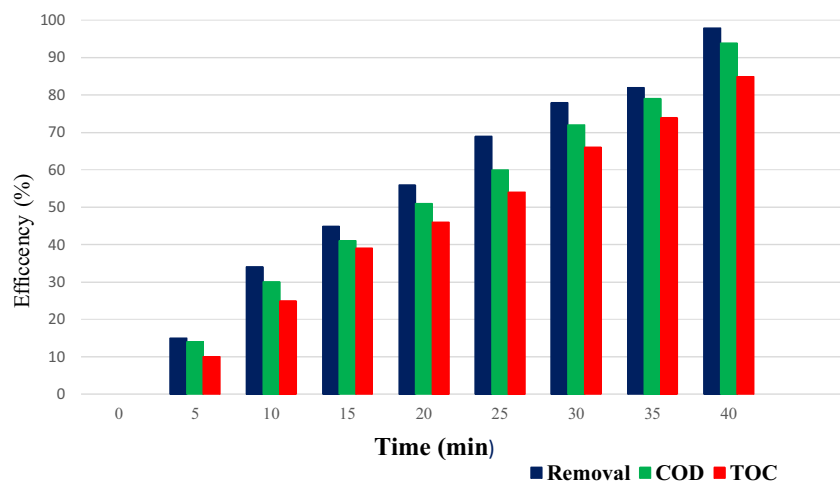


Fig. 8. Variations of TOC, COD and toluene removal efficiency during different irradiation times with 12% Ba doped BFO MNPs. ($t=25^\circ\text{C}$, CO (toluene) = 100 mg L^{-1} , CO (H_2O_2) = 0.65 mM , initial pH = 5.5).

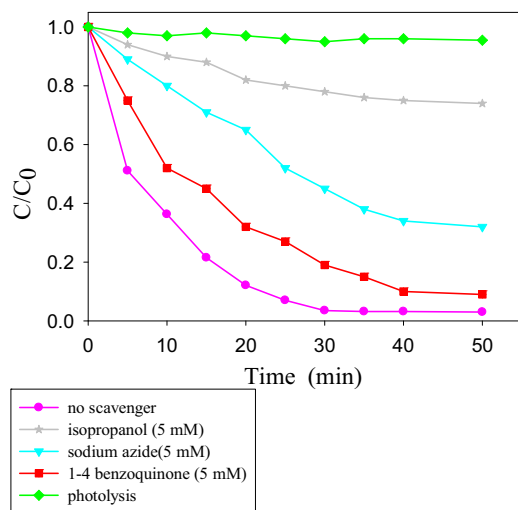


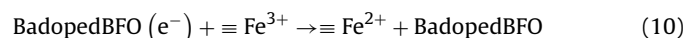
Fig. 9. Effect of different scavengers on the photocatalytic activity of 12% Ba doped BFO. ($t=25^\circ\text{C}$, CO (toluene) = 100 mg L^{-1} , CO (H_2O_2) = 0.6 mM , initial pH = 5.5).

decreased by about 71%, indicating that $\cdot\text{OH}$ is an important active radical intermediate involved in the photo-Fenton degradation of toluene. This fact also indicates that the reaction with the scavenger was not be completely quenched by IP, representing $\cdot\text{OH}$ is not the only species involved in toluene degradation. When 1–4 benzoquinone (1, 4-BQ) was added to the reaction solution as a scavenger of superoxide radical ($\text{O}_2^{\cdot-}$) [37], the photodegradation efficiency of toluene was slightly decreased by about 1%. The photodegradation efficiency of toluene was quenched about 29%, when sodium azide (NaN_3), a unique scavenger of singlet oxygen (${}^1\text{O}_2$) [38], was used to the reaction solution. This is indicated that the ${}^1\text{O}_2$ might be one of the active reaction intermediates in the photo-Fenton catalytic degradation of toluene. Our results identified that photo-Fenton degradation of toluene was mainly controlled by the formation characteristics of $\cdot\text{OH}$ and also partially affected by the formation of other active species such as $\text{O}_2^{\cdot-}$. Radical scavenger experiments and electron paramagnetic resonance spectroscopy proved that, $\text{O}_2^{\cdot-}$ played a key role in the photo-Fenton process of Rhodamine B with Fe-Co Prussian blue analogue [30].

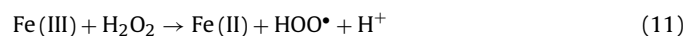
3.2.5. Proposed Fenton catalytic mechanism

Radical scavenger experiments demonstrated that $\text{O}_2^{\cdot-}$ was partly exhibited roles in the photo-Fenton catalysis process of toluene in addition to $\cdot\text{OH}$. Thus, the H_2O_2 decomposition promoted by undoped and Ba doped BFO by two possible reaction pathways: (i) via $\cdot\text{OH}$ mechanism and (ii) via $\text{O}_2^{\cdot-}$ reactions.

The Ba doped BFO MNPs is a narrow band gap photocatalyst. Thus, in addition to the generation of polycarboxylic acid as intermediates in dark and its effective role in the photo Fenton catalytic degradation of toluene in the presence of visible light via decomposition of H_2O_2 to produce $\cdot\text{OH}$ (Eqs. (2)–(5)), another path to generate $\cdot\text{OH}$ can be promised. When BFO or Ba doped BFO is illuminated with visible light, electrons can move from the valence band to the conduction band to give electron–hole pairs through reaction (Eq. (7)). Then, the dissolved oxygen can be as a photo generated electron scavenger to give $\text{O}_2^{\cdot-}$ (Eq. (8)). Finally, the photo-reduction of $\equiv\text{Fe}^{3+}$ to $\equiv\text{Fe}^{2+}$ takes place on the surface of Ba doped BFO MNPs under visible light according to Eqs. (9) and (10) [39]. Then, all of the formed $\equiv\text{Fe}^{2+}$ on the surface of Ba doped BFO MNPs can be reacted with H_2O_2 to produce $\cdot\text{OH}$ (Eq. (5)) [39]. The yield of $\equiv\text{Fe}^{2+}$ production is greatly increased with Ba substitution in BFO and also when $\equiv\text{Fe}^{3+}$ is complexed with carboxylic anion such as oxalate ions [40,41] that may be generated in the dark as an intermediate. Finally, toluene can be oxidized by generated $\cdot\text{OH}$ according to Eq. (6).



In the second mechanism, ${}^1\text{O}_2$ can also play a partial role in the photo Fenton catalytic degradation of the toluene. Thus, the series of reactions shown in Eqs. (11)–(18), can also participate in the photo-Fenton catalytic degradation of toluene under visible light, as $\cdot\text{OH}$ does in Eqs. (2)–(10).



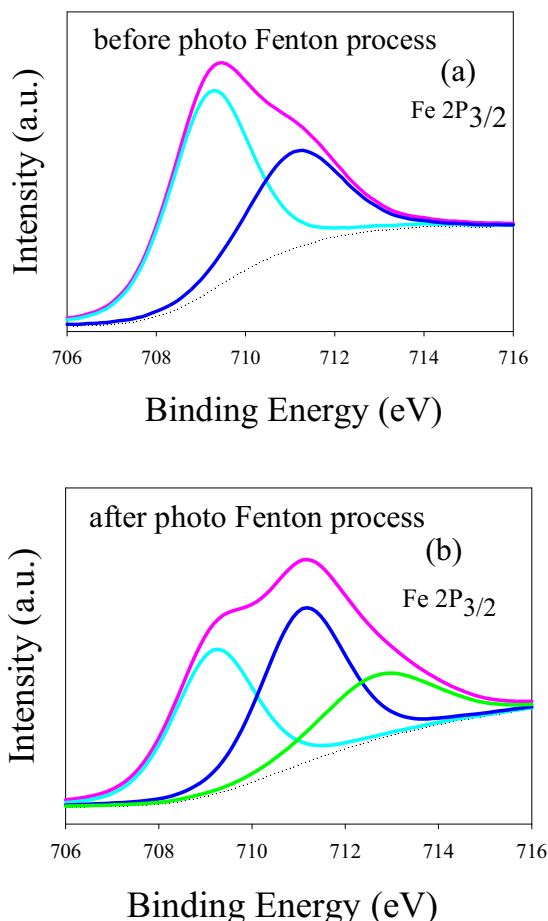
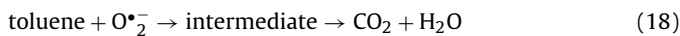
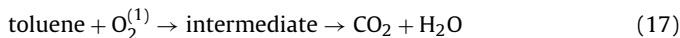


Fig. 10. High resolution XPS spectra of Fe 2p_{3/2} in 8% Ba doped BFO MNPs (a) before, and (b) after catalytic degradation process.



In these equations \bullet represents the sites on the solid surface. These results are in agreement with previously obtained results, in which singlet oxygen was identified by radical scavenger experiments and electron paramagnetic resonance spectroscopy for the photo-Fenton process of Rhodamine B with Fe-Co Prussian blue analogue [30].

3.2.6. Iron redox cycling and oxygens vacancies after photo-Fenton catalysis processes

The reduction of Fe³⁺ to Fe²⁺ species in 8% Ba doped BFO MNPs during photo-Fenton catalytic reaction was clearly shown in high resolution XPS spectra in Fig. 10a and b, in which, after photo-Fenton catalytic process, the Fe³⁺ proportion was somewhat increased. It means that the excellent photo-Fenton catalytic activity of Ba doped BFO mainly starts from Fe²⁺ and Fe³⁺ species on the surface of Ba doped BFO MNPs. This shift to higher binding energy value for Fe 2p orbit as an evident of the transformation of Fe²⁺ to Fe³⁺, has been reported earlier to promote

the oxidation of the water contaminants, ethinylestradiol (EE) and the model dye indigo carmine (IC) [42]. However, other study represented the opposite process, in which Fe³⁺ was reduced after the Fenton reaction [43].

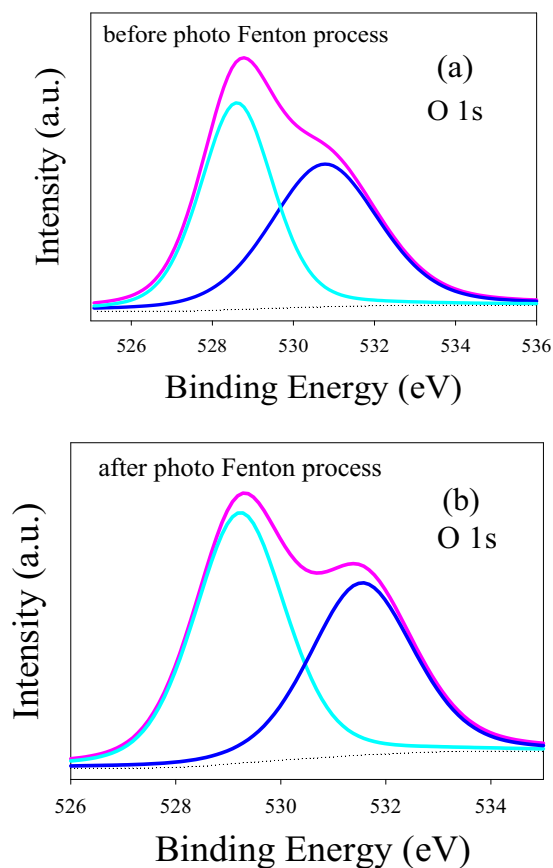


Fig. 11. High resolution XPS spectra of O 1s in 8% Ba doped BFO MNPs (a) before, and (b) after catalytic degradation process.

Fig. 11a and b shows the high resolution XPS spectra of O 1s in Ba doped BFO MNPs before and after catalysis process, respectively. As shown in Fig. 11 b, the binding energy of the O 1s peak becomes broader after photo-Fenton catalysis processes. This demonstrates that the existence of oxygen on the surface of Ba doped BFO had been affected by the visible light irradiation [30]. Furthermore, the new peak at 531.6 eV exhibited that the Fe–O species produced on the surface of the nanoparticles during the photo-Fenton process (Fig. 11b) [30,44]. The formation of new peak on the surface of Ba doped BFO MNPs at 531.6 eV, can be assigned the increase in contents of the Fe and O species during photo-Fenton process [43].

4. Conclusions

In this work, Bi_{1-x}Ba_xFeO₃ ($x=0.03, 0.08$ and 0.12) as visible-light photocatalysts were successfully synthesized via a simple and rapid sol-gel process. Then, the effect of Ba doping in BFO MNPs to increase the heterogeneous photo-Fenton catalytic degradation of toluene from aqueous solution was investigated. The great photo-Fenton catalytic activities of Ba doped BFO MNPs at a very weak acidic medium, pH = 5.5, are related to the existence of highly iron sites and abundant oxygen vacancies due to Ba loading, as compared to pure BFO MNPs. Radical scavenger experiments revealed the •OH as the main active species and ¹O₂ partly exhibited roles in the photo-Fenton catalytic degradation of toluene from aqueous solution. The efficient redox cycling of iron species and oxygen in the Ba doped BFO MNPs was deeply explored before and after photo-Fenton catalysis processes. The best catalytic efficiency of toluene with Bi_{1-x}Ba_xFeO₃ ($x=0.12$) was 98% photo degradation, 94% TOC and 85% COD reduction, respectively, after 40 min of visible irradiation at an initial pH of 5.5.

Acknowledgments

This work was financially supported through the project of the environmental technology development for chemical accident countermeasures funded by Korea Environmental Industry and Technology Institute, South Korea.

References

- [1] M.-S. Jo, E. Rene, S.-H. Kim, H.-S. Park, *World J. Microbiol. Biotechnol.* 24 (2008) 73–78.
- [2] E. Jindrová, M. Chocová, K. Demnerová, V. Brenner, *Folia Microbiol.* 47 (2002) 83–93.
- [3] T.-D. Pham, B.-K. Lee, *J. Hazard. Mater.* 300 (2015) 493–503.
- [4] T.-D. Pham, B.-K. Lee, C.-H. Lee, *Appl. Catal. B Environ.* 182 (2016) 172–183.
- [5] M.-R. Lee, C.-M. Chang, J. Dou, *Chemosphere* 69 (2007) 1381–1387.
- [6] J. Singh, B.-K. Lee, *J. Environ. Manag.* 161 (2015) 1–10.
- [7] F. Martínez, G. Calleja, J.A. Melero, R. Molina, *Appl. Catal. B Environ.* 60 (2005) 181–190.
- [8] E.G. Garrido-Ramírez, B.K.G. Theng, M.L. Mora, *Appl. Clay Sci.* 47 (2010) 182–192.
- [9] T. Soltani, M.H. Entezari, *Chem. Eng. J.* 251 (2014) 207–216.
- [10] T. Soltani, M.H. Entezari, *Chem. Eng. J.* 223 (2013) 145–154.
- [11] T. Soltani, M.H. Entezari, *J. Mol. Catal. A Chem.* 377 (2013) 197–203.
- [12] T. Soltani, M.H. Entezari, *Ultrason. Sonochem.* 20 (2013) 1245–1253.
- [13] W. Luo, Y.-S. Li, J. Yuan, L. Zhu, Z. Liu, H. Tang, S. Liu, *Talanta* 81 (2010) 901–907.
- [14] W. Luo, L. Zhu, N. Wang, H. Tang, M. Cao, Y. She, *Environ. Sci. Technol.* 44 (2010) 1786–1791.
- [15] J. An, L. Zhu, Y. Zhang, H. Tang, *J. Environ. Sci.* 25 (2013) 1213–1225.
- [16] N. Wang, L. Zhu, M. Lei, Y. She, M. Cao, H. Tang, *ACS Catal.* 1 (2011) 1193–1202.
- [17] Z. Song, N. Wang, L. Zhu, A. Huang, X. Zhao, H. Tang, *Chem. Eng. J.* 198–199 (2012) 379–387.
- [18] M.M. Shirodkar, C. Hao, X. Dong, T. Guo, L. Zhang, M. Li, H. Wang, *Nanoscale* 6 (2014) 4735–4744.
- [19] B. Bhushan, A. Basumallick, S.K. Bandopadhyay, N.Y. Vasanthacharya, D. Das, *J. Phys. D Appl. Phys.* 42 (2009) 065004.
- [20] P. Li, Y.-H. Lin, C.-W. Nan, *J. Appl. Phys.* 110 (2011) 033922.
- [21] R. Das, S. Sharma, K. Mandal, *J. Magn. Magn. Mater.* 401 (2016) 129–137.
- [22] F. Azough, R. Freer, M. Thrall, R. Cernik, F. Tuna, D. Collison, *J. Eur. Ceram. Soc.* 30 (2010) 727–736.
- [23] F.Z. Qian, J.S. Jiang, S.Z. Guo, D.M. Jiang, W.G. Zhang, *J. Appl. Phys.* 106 (2009) 084312.
- [24] G. Dhir, G.S. Lotey, P. Uniyal, N.K. Verma, *J. Mater. Sci. Mater. Electron.* 24 (2013) 4386–4392.
- [25] G.C.M. Rodríguez, R. Ochrombel, B. Saruhan, *J. Eur. Ceram. Soc.* 28 (2008) 2611–2616.
- [26] J. Liqiang, S. Xiaojun, X. Baifu, W. Baiqi, C. Weimin, F. Honggang, *J. Solid State Chem.* 177 (2004) 3375–3382.
- [27] C.H. Yang, J. Seidel, S.Y. Kim, P.B. Rossen, P. Yu, M. Gajek, Y.H. Chu, L.W. Martin, M.B. Holcomb, Q. He, P. Maksymovych, N. Balke, S.V. Kalinin, A.P. Baddorf, S.R. Basu, M.L. Scullin, R. Ramesh, *Nat. Mater.* 8 (2009) 485–493.
- [28] V.A. Khomchenko, D.A. Kiselev, J.M. Vieira, A.L. Khoklin, M.A. Sá, Y.G. Pogorelov, *Appl. Phys. Lett.* 90 (2007) 242901.
- [29] G.S. Arya, N.S. Negi, *J. Phys. D Appl. Phys.* 46 (2013) 095004.
- [30] X. Li, J. Liu, A.I. Rykov, H. Han, C. Jin, X. Liu, J. Wang, *Appl. Catal. B Environ.* 179 (2015) 196–205.
- [31] T. Soltani, B.-K. Lee, *J. Hazard. Mater.* 316 (2016) 122–133.
- [32] W. Luo, L. Zhu, N. Wang, H. Tang, M. Cao, Y. She, *Environ. Sci. Technol.* 44 (2010) 1786–1791.
- [33] S. Irmak, H.I. Yavuz, O. Erbatur, *Appl. Catal. B Environ.* 63 (2006) 243–248.
- [34] A.R. Khataee, M. Zarei, R. Ordikhani-Seyedlar, *J. Mol. Catal. A Chem.* 338 (2011) 84–91.
- [35] J. Nguyen, Y. Ma, T. Luo, R.G. Bristow, D.A. Jaffray, Q.-B. Lu, *Proc. Natl. Acad. Sci. U. S. A.* 108 (2011) 11778–11783.
- [36] N. Dubey, S.S. Rayalu, N.K. Labhsetwar, R.R. Naidu, R.V. Chatti, S. Devotta, *Appl. Catal. A* 303 (2006) 152–157.
- [37] M. Yin, Z. Li, J. Kou, Z. Zou, *Environ. Sci. Technol.* 43 (2009) 8361–8366.
- [38] L. Ge, J. Chen, X. Qiao, J. Lin, X. Cai, *Environ. Sci. Technol.* 43 (2009) 3101–3107.
- [39] K.A. Hislop, J.R. Bolton, *Environ. Sci. Technol.* 33 (1999) 3119–3126.
- [40] C. Wang, H. Liu, Z. Sun, *Int. J. Photoenergy* 2012 (2012) 10.
- [41] W. Song, W. Ma, J. Ma, C. Chen, J. Zhao, Y. Huang, Y. Xu, *Environ. Sci. Technol.* 39 (2005) 3121–3127.
- [42] A.D. Purceno, A.P.C. Teixeira, A.B. Souza, J.D. Ardisson, J.P. de Mesquita, R.M. Lago, *Appl. Clay Sci.* 69 (2012) 87–92.
- [43] X.-J. Yang, X.-M. Xu, J. Xu, Y.-f. Han, *J. Am. Chem. Soc.* 135 (2013) 16058–16061.
- [44] D. Ivezović, H.V. Trbić, R. Peter, M. Petrávić, M. Čeh, B. Pihlar, *Electrochim. Acta* 78 (2012) 452–458.